ADVANCES IN ATMOSPHERIC SCIENCES, VOL. 34, AUGUST 2017, 952–964

• **Original Paper** •

Grid-cell Aerosol Direct Shortwave Radiative Forcing Calculated Using the SBDART Model with MODIS and AERONET Observations: An Application in Winter and Summer in Eastern China

Yunfei FU*[1,2], Jiachen ZHU[1], Yuanjian YANG[1,2], Renmin YUAN[1], Guosheng LIU[1,4], Tao XIAN[1], and Peng LIU[1,3]

[1]*School of Earth and Space Sciences, University of Science and Technology of China, Hefei* 230026*, China*

[2]*Key Laboratory of Atmospheric Sciences and Satellite Remote Sensing of Anhui Province, Anhui Institute of Meteorological Sciences, Hefei* 230031*, China*

[3]*Anhui Academy for Environmental Science Research, Hefei* 230071*, China*

[4]*Department of Earth, Ocean and Atmospheric Science, Florida State University, Tallahassee, Florida FL* 32306-4520*, USA*

(Received 31 August 2016; revised 7 February 2017; accepted 9 February 2017)

ABSTRACT

Taking winter and summer in eastern China as an example application, a grid-cell method of aerosol direct radiative forcing (ADRF) calculation is examined using the Santa Barbara DISORT Atmospheric Radiative Transfer (SBDART) model with inputs from MODIS and AERONET observations and reanalysis data. Results show that there are significant seasonal and regional differences in climatological mean aerosol optical parameters and ADRF. Higher aerosol optical depth (AOD) occurs in summer and two prominent high aerosol loading centers are observed. Higher single scattering albedo (SSA) in summer is likely associated with the weak absorbing secondary aerosols. SSA is higher in North China during summer but higher in South China during winter. Aerosols induce negative forcing at the top of the atmosphere (TOA) and surface during both winter and summer, which may be responsible for the decrease in temperature and the increase in relative humidity. Values of ADRF at the surface are four times stronger than those at the TOA. Both AOD and ADRF present strong interannual variations; however, their amplitudes are larger in summer. Moreover, patterns and trends of ADRF do not always correspond well to those of AOD. Differences in the spatial distributions of ADRF between strong and weak monsoon years are captured effectively. Generally, the present results justify that to calculate grid-cell ADRF at a large scale using the SBDART model with observational aerosol optical properties and reanalysis data is an effective approach.

Key words: aerosol direct radiative forcing, AERONET, MODIS, SBDART model

Citation: Fu, Y. F., J. C. Zhu, Y. J. Yang, R. M. Yuan, G. S. Liu, T. Xian, and P. Liu, 2017: Grid-cell aerosol direct shortwave radiative forcing calculated using the SBDART model with MODIS and AERONET observations: An application in winter and summer in eastern China. *Adv. Atmos. Sci.*, **34**(8), 952–964, doi: 10.1007/s00376-017-6226-z.

1. Introduction

Atmospheric aerosols, a multiphase system that consists of suspended gas, liquid and solid particles, play non-negligible roles in climate change (Charlson et al., 1992; Ramanathan et al., 2001; Kaufman et al., 2002; Menon et al., 2002). By directly absorbing and scattering solar energy (Charlson et al., 1992; Haywood and Shine, 1997) or indirectly acting as cloud condensation or ice nuclei (Kaufman et al., 2005), aerosols can modulate the surface–atmosphere radiation budget, which may further influence cloud formation, precipitation, atmospheric stability and air quality (Jones et al., 1994; Zhao et al., 2006a, 2006b; Rosenfeld et al., 2007; Zhao et al., 2013a, 2013b; Zheng et al., 2015). Aerosol direct radiative forcing (ADRF), described as the change in the net radiation flux with and without aerosols under clear-sky conditions, remains one of the greatest uncertainties in climate change (Myhre et al., 2013) because of the complex spatial and temporal variations of aerosols.

Anthropogenic aerosol loading in eastern China (EC) has rapidly increased in response to the similarly rapid industrialization and urbanization in this region over the past two decades, which has caused serious environmental and climatic problems (Zhang et al., 2007). Detailed investigations have been carried out to characterize aerosol optical properties and their radiation effects based on ground-based measurements, satellites observations and model simulations (Mao et al., 2002; Kim et al., 2007; Li et al., 2007; Xia et al., 2007a, 2007b; Han et al., 2008; Li et al., 2010; Bel-

* Corresponding author: Yunfei FU
Email: fyf@ustc.edu.cn

louin et al., 2013; Chen et al., 2013; Xia et al., 2016). Some studies have pointed out the seasonal variations of aerosol properties. For example, based on Aerosol Robotic Network (AERONET) observations, Xia et al. (2007a, 2007b) found that aerosol loading was at its maximum during summer and its minimum during winter. Accordingly, seasonal variations in single scattering albedo (SSA) and asymmetry factor (ASY) were observed over southern China, with small values occurring during winter and larger values in summer. Kim et al. (2007) also pointed out that aerosol optical depth (AOD) over East Asia peaks in spring and minimizes in autumn and winter, as well as there being a peak of monthly mean AOD in June, based on Moderate Resolution Imaging Spectroradiometer (MODIS) data. Moreover, in EC, high AOD values are found. For aerosol radiative effects, Wang et al. (2002) studied the temporal and spatial variation of sulfate aerosol radiative forcing and found it to be highly related to those of anthropogenic sulfate. Wang et al. (2009) compared aerosol radiative forcing under four classic weather conditions in Beijing and found significant differences in aerosol radiative forcing among them due to different aerosol properties and meteorological conditions. In addition, Ju and Han (2013) used a regional climate model to simulate the spatial distributions of aerosol radiative forcing in strong and weak East Asian monsoon circulations and revealed that atmospheric circulations in summer are directly related to aerosols and their climatic effects over EC. As for aerosol climatic effects, more recently, Liao et al. (2015) used the WRF-Chem model to simulate the radiative forcing of aerosols and their impact on surface air temperature in EC on the synoptic scale. The results indicated that aerosols exert a considerable cooling effect on surface air temperature.

In order to obtain relatively reasonable ADRF at the regional or global scale, continuous measurements of aerosol optical properties from ground-based networks and satellites are required. Previous studies have shown that AERONET measurements are highly accurate in characterizing aerosols (Xia et al., 2016), and that MODIS observations can provide systematic retrievals of AOD on the regional and global scale (Li et al., 2003; Kim et al., 2007; Zheng et al., 2015). It is important to attempt to obtain the ADRF constrained by observational aerosol optical properties from these datasets.

In addition, previous simulations of the aerosol radiative effect have mainly been performed at the site scale, based on radiation transfer models with inputs from a small number of ground-based sites. The objective of our study is to calculate grid-cell ADRF based on the Santa Barbara DISORT Atmospheric Radiative Transfer (SBDART) model, together with grid-cell AOD data from MODIS, and SSA and ASY data from AERONET sites, in EC (26°–40°N, 110°–122°E) from 2006 to 2014. The periods of winter and summer are defined as December through February (DJF) and June through August (JJA), respectively. The seasonal and interannual variations of AOD and the seasonal variations of SSA and ASY are taken statistically using observations from MODIS and AERONET, respectively. Then, calculations of grid-cell ADRF at the top of the atmosphere (TOA) and the surface are performed based on simulations of the SBDART model. Furthermore, the relationships between ADRF and meteorological parameters (temperature, relative humidity), and the spatial patterns of ADRF between strong and weak monsoon circulations, are investigated and compared.

2. Data and methods

2.1. *MODIS data*

The main dataset used for ADRF calculation in this paper is the monthly averaged Collection 6 Level 3 AOD product at $1^\circ \times 1^\circ$ horizontal resolution, which is derived from the Terra/MODIS instrument (accessible from http://ladsweb.nascom.nasa.gov/data/search.html). Compared with ground-based networks, MODIS can provide long-term continuous observations for analysis of the spatial and temporal distribution of aerosols. Generally, the Collection 6 AOD has a good level of accuracy and is appropriate for climatic and environmental research (Levy et al., 2010; Lyapustin et al., 2014).

To obtain the surface albedo, the dataset of the MCD43 albedo product is used. This product is a 16-day averaged Level 3 combined dataset containing observations from Terra and Aqua satellites at a horizontal resolution of 0.05°. To match the MODIS AOD data, the shortwave broadband black-sky albedo from the MCD43 product is grouped into a monthly $1^\circ \times 1^\circ$ longitude–latitude grid box dataset. The monthly mean albedo is defined as an average including all the data where the 16-day measurement period overlapped with the month of interest (Sundström et al., 2015). Moreover, a 1°-grid monthly dataset of albedo at AOD spatial resolution was established by a weight-averaged method, which picks the mean value of albedo at AOD grids.

2.2. *AERONET data*

To obtain aerosol optical properties, datasets (http://aeronet.gsfc.nasa.gov) derived from AERONET observations are used. AERONET is a ground-based remote sensing aerosol network established by NASA and PHOTONS (PHOtométrie pour le Traitement Opérationnel de Normalisation Satellitaire) (Holben et al., 1998; Dubovik et al., 2000), which issues a freely available database of accurate aerosol optical properties.

Based on the CIMEL CE-318 sun photometer, the multichannel automatic scanning radiometer, AERONET measures AOD at the wavelengths of 340, 380, 440, 500, 675, 870 and 1020 nm, and provides inversion products such as SSA, ASY, and complex refractive index at 440, 670, 870 and 1020 nm (Dubovik and King, 2000; Dubovik et al., 2002). These products are derived for three data quality levels: Level 1.0 (unscreened); Level 1.5 (cloud-screened); and Level 2.0 (cloud-screened and quality-assured).

AERONET observations have been, and continue to be, widely used to characterize aerosol optical properties and their radiative effects (Kim et al., 2007; Xia et al., 2007a, 2007b, 2016; Wang et al., 2009; Chen et al., 2013; Sundström et al., 2015). In the present study, due to the limited

spatial distribution of AERONET sites in China, five available sites with relatively abundant observations are selected to spatially represent the status in EC (Table 1). The Version 2, Level 2 monthly averaged SSA and ASY data from these sites, together with AOD provided by MODIS, are used to analyze aerosol optical properties, and are imported into the SBDART model to estimate ADRF.

2.3. *Meteorological data*

To create atmospheric profiles for the SBDART model, the ozone mixing ratio, specific humidity and temperature at 37 pressure levels (1, 2, 3, 5, 7, 10, 20, 30, 50, 70, and 100 to 250 by 25, 300 to 750 by 50, and 775 to 1000 by 25 hPa) are used in the study. The total column ozone and total column water vapor data are also employed as inputs of the model. Moreover, temperature and relative humidity at 1000 hPa are used to investigate the relationships between ADRF and meteorological parameters. Wind vectors at 850 hPa and geopotential height at 500 hPa are employed to analyze the relationships between ADRF and monsoon circulations. All these data are extracted from the European Centre for Medium-Range Weather Forecasts (ECMWF) reanalysis dataset, on a $1.0^\circ \times 1.0^\circ$ latitude/longitude grid, on a monthly basis.

2.4. *SBDART model*

To estimate ADRF, the SBDART model is adopted, which calculates plane-parallel radiative transfer within the atmosphere and at the Earth's surface (Ricchiazzi et al., 1998). The calculation includes all important processes that affect the ultraviolet, visible and infrared radiation fields. SBDART is scripted in the FORTRAN language and is a marriage of a discrete ordinate radiative transfer module, low-resolution atmospheric transmission model, and Mie scattering results for light scattering by water droplets and ice crystals.

The main input file of SBDART is called INPUT, where users can define about 60 parameters and 12 output options, including atmospheric profiles, aerosol types, surface types and cloud properties. In fact, SBDART contains six standard atmospheric profiles, five basic surface types, four standard aerosol types, and vertical distribution models of aerosols, which offer users default values for input parameters; however, users can also specify real values of these parameters. In this study, the SBDART model is used for ADRF simulation.

Table 1. Details of the AERONET sites used in the present study.

Region	Site name	Latitude (°N)	Longitude (°E)	Elevation (m)	Observation period
NEC	Beijing	39.977	116.381	92	2001.03–2015.02
	Xianghe	39.754	116.962	36	2001.03–2015.02
	Xinglong	40.396	117.578	970	2006.02–2012.05
SEC	Taihu	31.421	120.215	20	2005.09–2012.10
	Hefei	31.905	117.162	36	2005.11–2008.11

2.5. *Methods*

The aerosol optical properties (AOD from MODIS; SSA and ASY from AERONET), surface reflectance (surface albedo from MODIS), atmospheric profiles (temperature, pressure, ozone mixing ratio and specific humidity from ECMWF), and total column ozone and water vapor provided by ECMWF, are used as the input parameters for the SBDART model in the ADRF simulations. Specifically, we begin by running the ADRF simulation on the MODIS grid and in the shortwave spectral region (0.25–4 μm), because shortwave ADRF is more significant than longwave ADRF (Shi et al., 2008). According to Xia et al. (2016), in southeastern and northeastern China, there are different predominant aerosol types and different proximities to source areas, so we divide EC into two parts: northeastern China (NEC) and southeastern China (SEC). Accordingly, AERONET sites are grouped into two categories: the sites at Beijing, Xianghe and Xinglong represent the environment of NEC, while the sites of Hefei and Taihu—situated in the Yangtze River Delta region—represent the environment of SEC. Then, we calculate the site-averaged SSA and ASY for each part. In different parts we use different SSAs and ASYs, while for a given part we consider them unchanged between different MODIS grids. However, the AOD, surface albedo, total column ozone and water vapor change among these different MODIS grids. In addition, the atmospheric profile, surface albedo, water vapor and ozone will be the same for aerosol and non-aerosol calculations. Other input parameters (volume mixing ratios of certain gases, such as N_2, O_2, CO_2, CH_4) in the calculations are generated from the midlatitude climatic mean database in SBDART. A schematic diagram of the radiative calculation processes employed to simulate ADRF in this study is shown in Fig. 1. The main outputs of

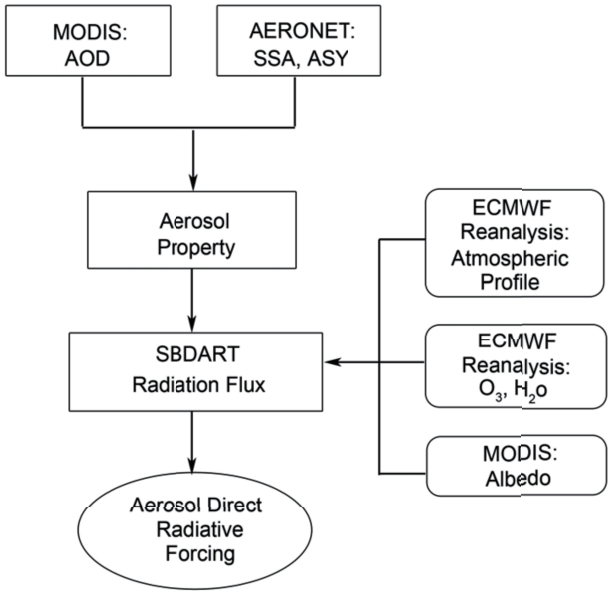

Fig. 1. Schematic diagram of the radiative calculation processes employed in this study to simulate aerosol direct radiative forcing.

the simulations are downward and upward fluxes at the TOA and at the surface.

The formulas used for the calculation of ADRF are as follows:

$$\Delta F = F^{\downarrow} - F^{\uparrow}\ ; \tag{1}$$

$$\Delta F_{\mathrm{TOA}} = \Delta F_{\mathrm{aero,TOA}} - \Delta F_{\mathrm{non\text{-}aero,TOA}}\ ; \tag{2}$$

$$\Delta F_{\mathrm{SFC}} = \Delta F_{\mathrm{aero,SFC}} - \Delta F_{\mathrm{non\text{-}aero,SFC}}\ ; \tag{3}$$

where ΔF is the net flux (downward radiation minus upward radiation); the subscripts "TOA" and "SFC" indicate the top of the atmosphere and surface, respectively; and the subscripts "aero" and "non-aero" represent the condition with and without aerosol, respectively.

3. Results

Previous studies have suggested that the spatial distribution of ADRF is highly reliant on that of aerosol optical properties, i.e., SSA, ASY and AOD (Wang et al., 2002; Ju and Han, 2013). Therefore, prior to the simulation of ADRF, we first need to gain a full picture of these parameters. To justify the ADRF results calculated by the approach employed in this study, spatial and temporal variations of aerosol radiative effects in EC are then explored. Moreover, the relationships between ADRF and both meteorological parameters and monsoon activity are examined.

3.1. *Spatial and temporal variations of aerosol optical properties and ADRF*

Firstly, based on AERONET observations, the temporal and spatial characteristics of SSA and ASY over EC are calculated for the period 2006–2014. As shown in Table 2, it is clear that there are distinct seasonal variations of SSA and ASY. During winter, the SSA (ASY) values at 440, 670, 870 and 1020 nm are all smaller than those during summer, in both NEC and SEC, due to the burning of coal for heating in NEC and industrial activities in SEC (Chen et al., 2013). The higher SSA in summer is likely associated with the formation of larger amounts of secondary aerosols and the increasing hydroscopicity of fine particles caused by high humidity, leading to a weakening in the absorption capacity of aerosols (Xia et al., 2007a, 2007b; Chen et al., 2013). According to the definition of SSA (the ratio of scattering efficiency to total extinction efficiency), the larger the value of SSA, the stronger the scattering ability of the aerosol. Similarly, the larger the value of ASY, the greater the amount of forward scattering occurs. Therefore, it can be concluded that aerosols present stronger scattering and may exhibit more forward scattering in summer than in winter. As for the regional differences during winter, the SSA in NEC is smaller than that in SEC due to the increased amounts of black carbon aerosols caused by coal burning, which is opposite in summer.

Table 2. Aerosol optical properties during winter and summer in EC.

Region	Wavelength (nm)	Winter SSA	Summer SSA	Winter ASY	Summer ASY
NEC	440	0.879	0.944	0.693	0.719
	670	0.907	0.946	0.645	0.668
	870	0.898	0.941	0.633	0.642
	1020	0.889	0.937	0.632	0.635
SEC	440	0.887	0.934	0.721	0.737
	670	0.908	0.931	0.690	0.672
	870	0.901	0.926	0.636	0.633
	1020	0.896	0.922	0.628	0.619

For a better comprehension of the AOD differences, Fig. 2a shows the spatial patterns of the climatological mean AOD in winter and summer over EC for the same period (2006–

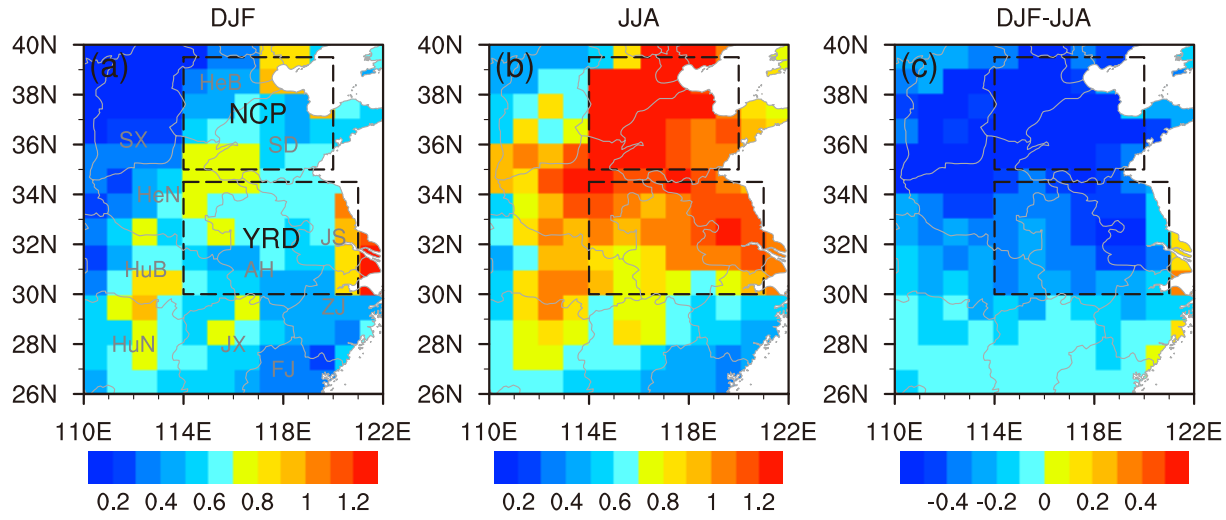

Fig. 2. Spatial patterns of climatological mean AOD in (a) winter (DJF), (b) summer (JJA), and (c) their difference (DJF minus JJA), viewed by Terra/MODIS over EC during 2006–2014. Two sub-regions (the NCP and YRD) are indicated by the boxes. Gray letters in (a) indicate the provinces of Shanxi (SX), Shandong (SD), Hebei (HeB), Henan (HeN), Hubei (HuB), Hunan (HuN), Anhui (AH), Jiangxi (JX), Jiangsu (JS), Zhejiang (ZJ), and Fujian (FJ).

2014) as that of the AERONET observations. The data indicate that the AOD ranges from 0.3 to 0.7 in winter for the entire EC area, and three distinct centers in SEC are observed with relatively high AOD values: the junction of Anhui and Henan provinces; parts of Jiangsu Province; and parts of Hubei and Hunan provinces. In summer, however, the spatial pattern of AOD is different from that in winter (Fig. 2b). The AOD values are between 0.5 and 1.2, and we can see that both the North China Plain (NCP) and the Yangtze River Delta (YRD)—areas considered to be the most developed in EC—are centers of high AOD (larger than 1.0). As for the seasonal differences (Fig. 2c), negative values are apparent across EC, which means that the AOD is larger in summer and smaller in winter. The higher AOD in summer is likely attributable to a variety of processes, such as secondary aerosol formation and the hygroscopic growth of fine particles and smoke aerosols caused by regional crop residue burning (Kim et al., 2007; Xia et al., 2007a, 2016; Cheng et al., 2014). Meanwhile, the smaller AOD in winter in NEC is mainly due to the dispersion effect caused by synoptic processes, such as the passage of cold fronts (Li et al., 2007; Xia et al., 2016). Also, the seasonal variations in NEC are more significant than those in SEC.

Based on the above results, two sub-regions are selected owing to their prominence as high aerosol loading centers and their control by different aerosol sources and aerosol types: NEC, including the NCP (35°–40°N, 114°–120°E); and SEC, including the YRD (30°–35°N, 114°–121°E).

According to the formulas of ADRF calculation mentioned in section 2.5, the spatial pattern results for the climatological mean ADRF in winter and summer over EC are shown in Fig. 3. It is clear that aerosols induce negative forcing at the TOA in both winter and summer over the entire study region, wherein the calculated values of ADRF change from −20 W m^{-2} to −45 W m^{-2}. It is also obvious that the cooling center of aerosol in winter is located in South China, since the AOD and SSA values are higher in this area. In summer, meanwhile, the cooling center occurs in North China, especially over the NCP, due to the strong scattering and higher AOD in this region. Therefore, the seasonal differ-

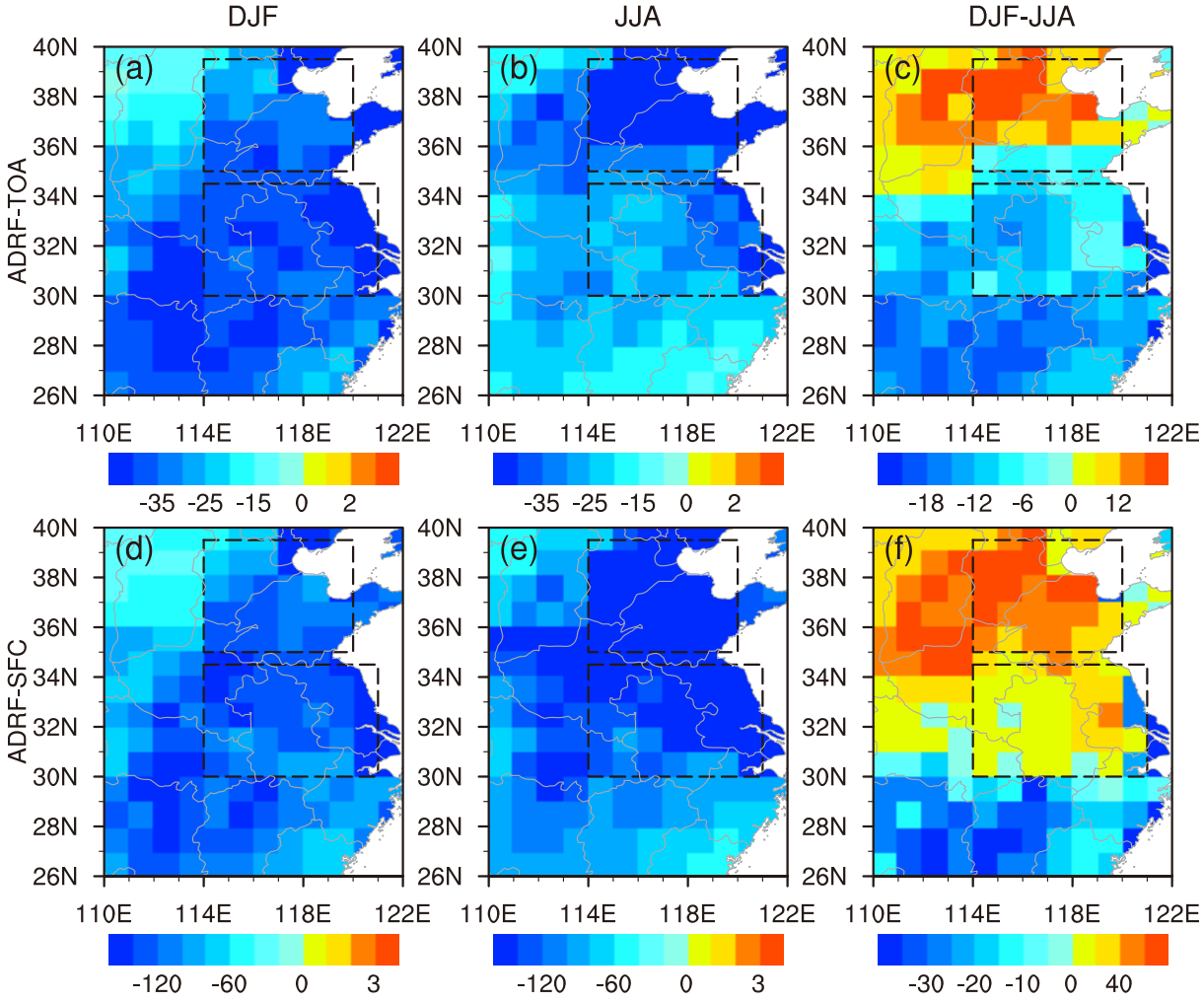

Fig. 3. Spatial patterns of climatological mean ADRF (units: W m^{-2}) at the (a–c) TOA and (d–f) surface (SFC), in (a, d) winter (DJF) and (b, e) summer (JJA), and (c, f) their differences (DJF minus JJA), in EC during 2006–2014. The boxes represent the same sub-regions as detailed in Fig. 2.

ences of ADRF vary between areas. Over the NCP, aerosols produce weaker negative forcing in winter than in summer owing to the absorption of aerosols, and lower AOD values during winter. For the other areas, however, the ADRFs are stronger in winter than in summer, as plotted in Fig. 3c.

Similar to the spatial patterns of ADRF at the TOA, aerosols generate negative forcing at the Earth's surface over the entire study area during both winter and summer, as shown in Figs. 3d and e. Generally, the calculated values of ADRF vary from −40 W m^{-2} to −140 W m^{-2} in winter and from −60 W m^{-2} to −160 W m^{-2} in summer, which are four times stronger than those at the TOA. This result is significant as it demonstrates a clear direct forcing effect of aerosols in EC. In addition, two strong cooling centers are located in the YRD and NCP during winter and summer, which is different from the distribution of ADRF at the TOA. In terms of seasonal differences, the aerosol cooling effects are stronger in summer in both the NCP and YRD, whereas the opposite effect is observed in the other areas, as shown in Fig. 3f.

To identify the trends of ADRF in EC, which is an issue of wide concern in climate change research, Fig. 4 shows the time series of AOD and ADRF at the TOA and the surface in EC and its two sub-regions in winter and summer. In general, it is clear that the AOD and ADRF at the TOA and the surface present strong interannual variations throughout the research areas in winter and summer. Figures 4a and d show that the regional mean AOD presents weak upward trends in winter and downward trends in summer. Both figures also show that the amplitude of AOD in summer is larger than that in winter, which suggests that the interannual variability of AOD is greater in summer. This is likely associated with the occasional occurrence of biomass burning in summer (Xia et al., 2016). Moreover, in summer (Fig. 4d), the variation and amplitude of AOD in the two sub-regions exhibit non-significant regional differences; while in winter (Fig. 4a), values of AOD over the NCP are much lower than those for the YRD. Furthermore, the pattern of interannual variability for AOD over EC is almost the same as that over its two sub-regions. The ADRF at the TOA presents a decreasing trend in both winter and summer over EC, the NCP and the YRD (Figs. 4b and e). However, the ADRF at the surface shows a decreasing trend during winter and an increasing trend in summer (Figs. 4c and f). Furthermore, similar to those for the AOD, the variation and amplitude of ADRF at the TOA and the surface are greater in summer, and regional discrepancies between the two sub-regions are more remarkable in winter.

Generally, ADRF is highly correlated with AOD, and if there is an upward trend of AOD (increasing values of AOD) there will be a downward trend of ADRF (decreasing values of ADRF), which means that higher AODs will cause stronger aerosol cooling effects. However, aside from AOD, the SSA of aerosol is also found to be a dominant factor with

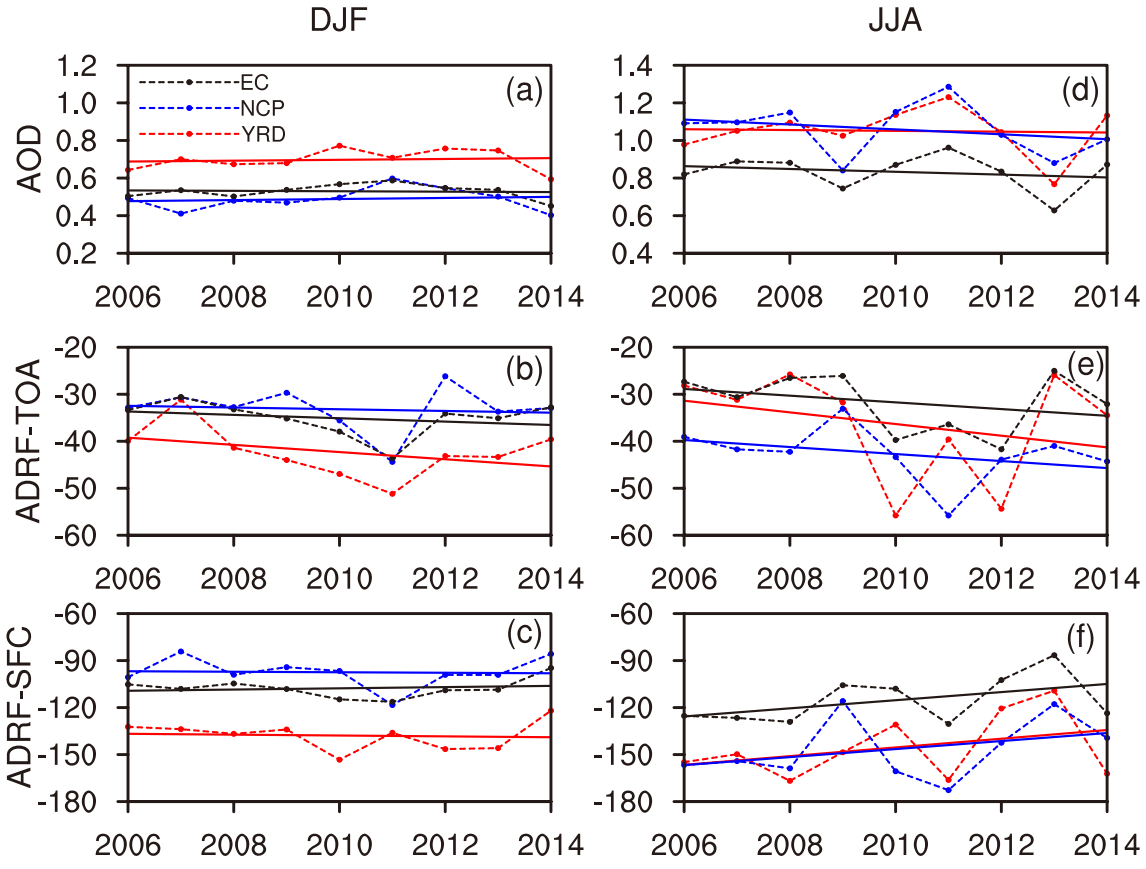

Fig. 4. Time series of (a, d) AOD and (b, c, e, f) ADRF (units: W m^{-2}) over EC and its sub-regions (the NCP and YRD) during (a–c) winter and (d–f) summer for the period 2006–2014. The solid lines are fitted linear trend lines.

respect to the interannual variations of ADRF, which will directly affect the trends of ADRF. Xia et al. (2016) identified the relationships between ADRF and both AOD and SSA and found that AOD and SSA can determine >94% and >87% of the ADRF variability, respectively. Therefore, it is clear that the trends of ARF do not always correspond well to those of AOD, as shown in Fig. 4.

It is also apparent from Fig. 4 that the interannual patterns of ADRF are opposite to those of AOD, which indicates that high aerosol loading usually corresponds to strong negative forcing. However, there are some exceptions. For example, in the summer of 2011, AOD values peaks in this year over all three areas, which means that the ADRF should be lowest in this year (Fig. 4d). However, the ADRF at the TOA over the YRD is smaller than expected, because the SSA over the YRD in 2011 is much smaller than that in 2010 and 2012 (0.938 in 2011; 0.967 in 2010; and 0.970 in 2012).

3.2. *Relationships between ADRF and both meteorological parameters and monsoon activity*

In order to understand what causes differences in ADRF over EC in summer and winter, the relationships among ADRF, temperature and relative humidity are investigated in this section. Firstly, the time series of temperature and relative humidity for EC and its sub-regions in winter and summer are plotted in Fig. 5. It is clear that temperature and relative humidity present strong interannual variations in both winter and summer. However, the amplitudes of temperature and relative humidity are larger in winter, which equates to relatively strong interannual variations of temperature and relative humidity in winter. In addition, the patterns of variation with respect to temperature and relative humidity over EC and YRD are almost the same which is contrary to the lower variation in NCP.

To understand clearly the relationships between ADRF and both temperature and relative humidity, Table 3 lists the calculated correlation coefficients. The results indicate there is positive correlation between ADRF and temperature, which suggests that with the enhancement of the aerosol cooling effect there should be a decrease in temperature, as discussed in previous studies (Ju and Han, 2013; Liao et al., 2015; Zhang et al., 2016). Negative correlation is found between ADRF and relative humidity. The definition of relative humidity is the ratio of actual water vapor pressure to saturated vapor pressure. Negative ADRF will cause surface cooling, which decreases the value of saturated vapor pressure. Meanwhile, changes in actual water vapor depend on the water vapor flux from the ground to the air above. The negative correlation indicates that, with the strength of the aerosol cooling effect (decreasing ADRF), the relative humidity increases as a result of the saturated vapor pressure being decreased more than the actual pressure (Zhang et al., 2016).

Table 3. Correlation coefficients at the surface (SFC, 1000 hPa) between ADRF and both temperature and relative humidity, over EC and its sub-regions (NCP and YRD), during winter (December–February, DJF) and summer (June–August, JJA), for the period 2006–2014.

	Coefficents		
	EC	NCP	YRD
ADRF-T (DJF)	0.69**	0.21	0.37
ADRF-T (JJA)	0.66*	0.48	0.75**
ADRF-RH (DJF)	−0.26	0.17	0.15
ADRF-RH (JJA)	−0.72**	−0.43	−0.71**

*0.1 level of significance; **0.05 level of significance.

It is well known that the climate of EC has been strongly affected by summer and winter monsoon activities. Previous studies have indicated that monsoon circulations modulate

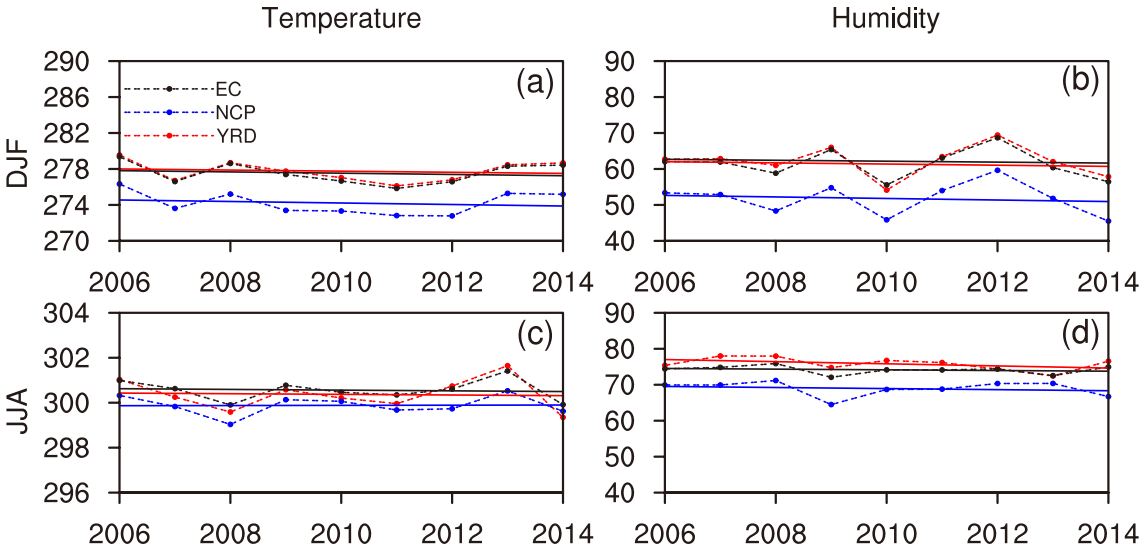

Fig. 5. Time series of (a, c) temperature (units: K) and (b, d) relative humidity (units: %) in EC and its sub-regions (the NCP and YRD) during (a, b) winter and (c, d) summer from 2006 to 2014. The solid lines are fitted linear trend lines.

the spatial patterns of aerosols and its radiation effects in East Asia (Zhang et al., 2003, 2010; Zhu, 2008; Zhu et al., 2012; Wu et al., 2016). Based on winter and summer East Asian monsoon indices (Li and Zeng, 2002; Zhu, 2008), we select two strong (2007, 2011) and two weak (2006, 2008) winter monsoon years, as well as two strong (2006, 2012) and two weak (2008, 2010) summer monsoon years, to explore the relationships among monsoon circulations, aerosols, and their induced radiative forcing in winter and summer in EC.

Prior to comparing the different spatial distributions of ADRF between strong and weak monsoon years, we first examine the differences in atmospheric circulations and the spatial patterns of AOD, as plotted in Fig. 6. During winter, the main feature of the wind field at 850 hPa is the dominant northwesterly flow that prevails over EC in both strong and weak monsoon years (Figs. 6a and b). However, compared with the weak monsoon years, the north wind component intensifies, which will effectively strengthen the southward transport of aerosols; and the west wind component weakens, which is not conducive to the outflow of aerosols in strong monsoon years (Fig. 6c). The geopotential height at 500 hPa indicates that EC is located behind the East Asian trough, which promotes northwesterly flow over EC in both strong and weak monsoon years (Figs. 6a and b). In addition, the East Asian trough becomes deeper in strong monsoon years, and negative geopotential height differences are present between strong and weak monsoon years (Fig. 6c).

Modulated by monsoon circulations, the corresponding spatial patterns of AOD are presented in Figs. 6d–f. As shown, the spatial distributions of AOD are almost the same between strong and weak monsoon years. However, influenced by the weakened northwesterly flow, the high aerosol loading centers, spreading across SEC, shift to NEC in weak monsoon years. As for the differences, in the YRD, the values of AOD are larger in strong monsoon years, which may be associated with the intensified northerly wind bringing greater amounts of aerosol to the area and the weakened westerly wind component preventing the outflow of aerosols. Meanwhile, larger values occur in weak monsoon years in parts of the NCP, which is likely attributable to the enhanced northerly wind helping to disperse aerosols in this area.

The corresponding spatial distributions of ADRF are presented in Figs. 6g–l. Similar to those of AOD, the spatial patterns of ADRF in strong and weak monsoon years are almost the same. However, under the influence of monsoon circulations and AOD, negative ADRF differences occur over almost all of EC, meaning aerosols induce stronger cooling effects in strong monsoon years. Positive ADRF differences center on areas with negative AOD differences.

The correlations between AOD, ADRF and monsoon index are shown in Table 4. We can see that AOD and ADRF are highly correlated with monsoon index in winter. Positive correlations are observed between AOD and monsoon index, and negative correlations between ADRF and monsoon index, which also suggests that AOD values are higher and the aerosol cooling effects are stronger in strong winter monsoon years.

Table 4. Correlation between East Asian monsoon index and both AOD and ADRF [at the surface (SFC) and at the TOA], over EC and its sub-regions (NCP and YRD), during winter (DJF) and summer (JJA), for the period 2006–2014.

	Coefficients		
	EC	NCP	YRD
AOD-DJF	0.73**	0.46	0.40
AOD-JJA	−0.10	−0.27	−0.11
ADRF-TOA-DJF	−0.65*	−0.48	−0.40
ADRF-TOA-JJA	−0.17	0.22	−0.16
ADRF-SFC-DJF	−0.66*	−0.42	−0.19
ADRF-SFC-JJA	0.10	0.22	0.11

*0.1 level of significance; **0.05 level of significance.

Similar to previous analyses about relationships between ADRF and winter monsoon circulations, we first consider the differences in atmospheric circulations and spatial distributions of AOD between strong and weak summer monsoon years. During strong summer monsoon years, the major characteristic of the 850 hPa wind field is that strong southerly flow prevails over EC, as shown in Fig. 7a. In contrast, during weak monsoon years, the principal feature of the wind field at 850 hPa is southwesterly flow (Fig. 7b). The main differences indicate that, during strong monsoon years, the zonal wind component weakens while the meridional wind component intensifies, which contributes to the northward transport of aerosols in those years (Fig. 7c). The geopotential height at 500 hPa indicates that a southwestward drift of the subtropical high occurs in weak monsoon years and negative geopotential height differences are found in EC (Fig. 7c). As a result, the spatial patterns of AOD change along with monsoon circulations. Relative to strong monsoon years, aerosol loading is higher in weak monsoon years, especially in the NCP and YRD, which is attributable to the weakened northerly wind in weak monsoon years reducing the northward transport of aerosols and generating favorable conditions for the accumulation of aerosols in this area (Fig. 7f).

Correspondingly, Figs. 7g–l present the spatial patterns of ADRF at the TOA and the surface during strong and weak summer monsoon years. As shown in the figure, the spatial distributions of ADRF at the TOA and the surface show similar patterns. During strong monsoon years (Figs. 7g and j), prominent negative forcing centers are located in the NCP and the YRD at both the TOA and the surface. In weak monsoon years (Figs. 7h and k), however, the cooling centers are stronger. As for the differences in ADRF between strong and weak years (Figs. 7i and l), the aerosol cooling effects in the sub-regions of EC (i.e., the NCP and YRD) are stronger during weak monsoon years due to the enhancement of AOD in these years, whereas the opposite situation is found in the other areas. Different from winter, negative correlation is found in summer between AOD and monsoon index, and positive correlation between ADRF and monsoon index, which indicates that higher aerosol loading will induce greater cool-

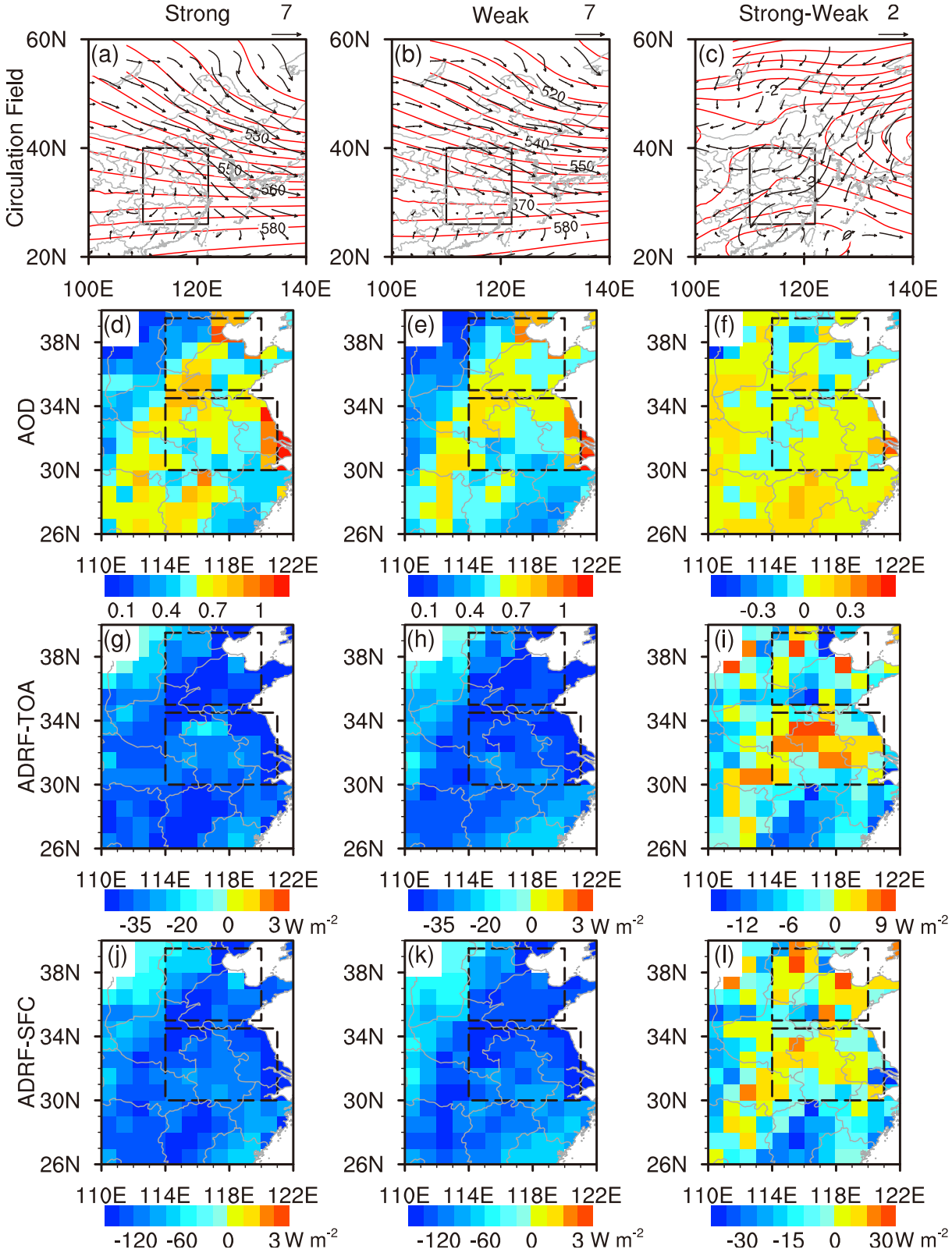

Fig. 6. Spatial distribution of the (a–c) 850 hPa wind field (vectors; units: m s^{-1}) and 500 hPa geopotential height field (red contours; units: 10 gpm), and the (d–f) AOD and (g–l) ADRF (units: W m^{-2}) at the (g–i) TOA and (j–l) surface (SFC), during (a, d, g, j) strong and (b, e, h, k) weak winter monsoon years, and (c, f, i, l) their differences (former minus latter). The black rectangular region in (a–c) represents EC (26°–40°N, 110°–122°E). The dashed black boxes in (d–l) are the same as in Fig. 2.

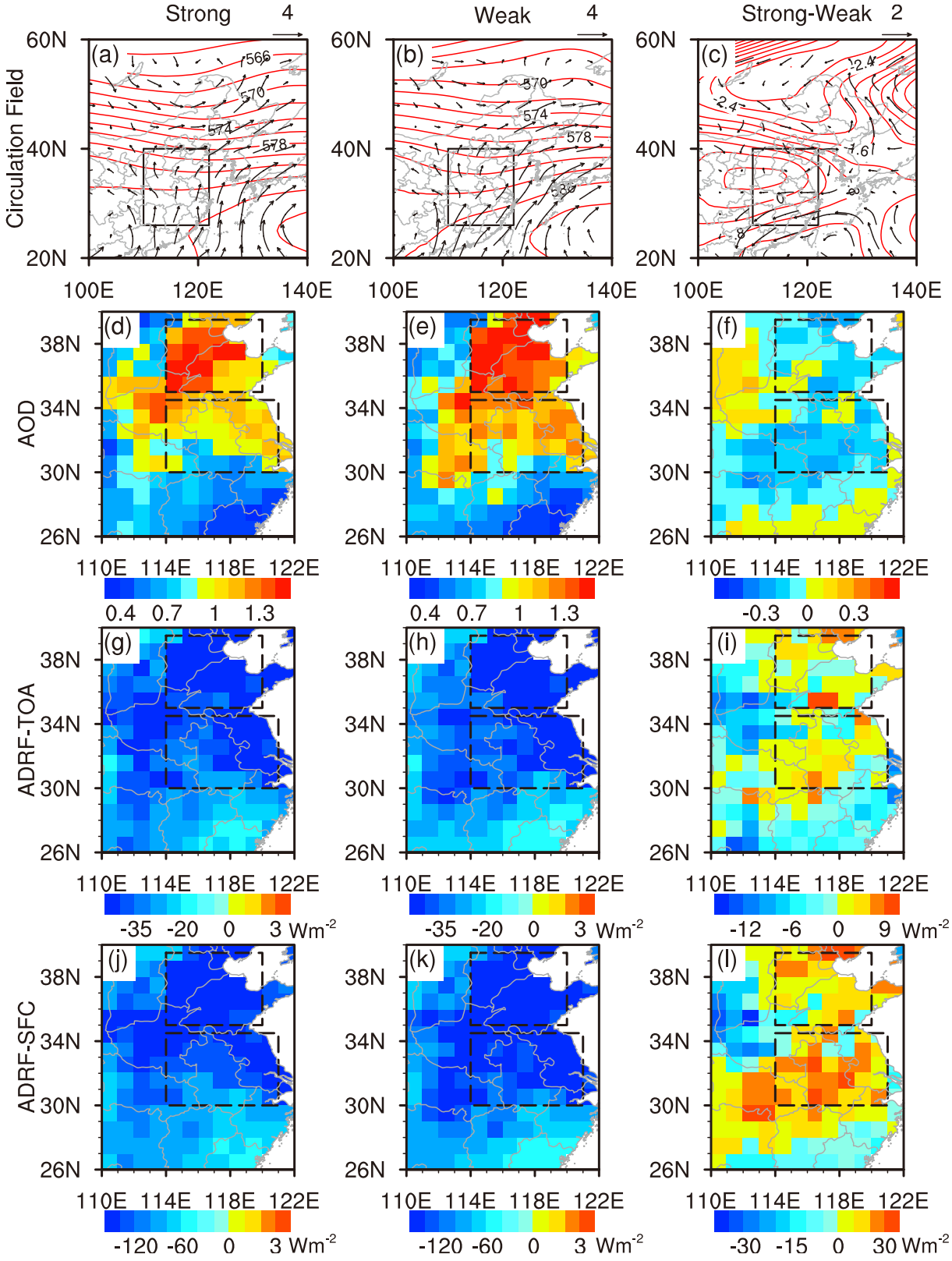

Fig. 7. As in Fig. 6, but for summer monsoon years.

ing effects in weak monsoon years (Table 4).

In general, monsoon circulations play critical roles in transporting aerosols and then changing the spatial patterns of the aerosol radiation effects in EC in both winter and summer, which is consistent with previous results (Zhu et al., 2012; Ju and Han, 2013).

4. Summary and discussion

The present study introduces a new approach for calculating grid-cell ADRF based on the SBDART model together with observations from MODIS and AERONET and reanalysis data. To justify the ADRF results calculated using this new approach, we begin by exploring the spatial and temporal variations of aerosol optical properties and aerosol radiative effects in EC, and then examine the relationships between ADRF and both temperature and relative humidity. Finally, the spatial distributions of AOD and ADRF are compared between strong and weak monsoon years. The major results and conclusions can be summarized as follows:

Distinct seasonal and regional variations of aerosol properties and ADRF are observed. During winter, SSAs at different wavelengths are all smaller than those in summer due to the burning of coal for heating in NEC and industrial activities in SEC. The higher SSA in summer is likely associated with the formation of larger amounts of secondary aerosols and the increasing hydroscopic growth of fine particles. SSA is higher in North China in summer, but in South China higher SSA occurs during winter. Higher AOD occurs in summer due to biomass burning, and two prominent high aerosol loading centers are observed. Smaller AOD values in winter in NEC are mainly due to the dispersion effect caused by synoptic processes. Aerosols induce negative forcing at the TOA and the surface during both winter and summer, which may be responsible for the decrease in surface temperature and the increase in relative humidity. Values of ADRF vary from -40 W m^{-2} to -140 W m^{-2} at the surface, which are four times stronger than those at the TOA. Seasonal differences of ADRF are regionally dependent.

Both AOD and ADRF present strong interannual variations; however, their amplitudes are larger in summer as a result of occasional biomass burning at that time of year. Moreover, modulated by SSA, the patterns and trends of ADRF do not always correspond well to those of AOD.

There are significant differences in the spatial distributions of AOD and ADRF between strong and weak monsoon years. Aerosols will induce stronger cooling effects in strong winter monsoon years and in weak summer monsoon years, which implies that the intensity of monsoon circulations have a direct relationship with the transportation of aerosols and their radiative effects.

The objective of our study is to calculate grid-cell aerosol direct ADRF on the regional scale based on the simulation of the SBDART model with inputs of reliable AOD data from MODIS, and SSA and ASY data from AERONET sites. Compared to previous results (Xia et al., 2007a, 2007b, 2016; Wang et al., 2009; Ju and Han, 2013), the values of ADRF in our study are reasonable, as are the seasonal and interannual variations and spatial patterns of ADRF, which suggests that the method employed in our study is effective for evaluating grid-cell aerosol radiation effects at the regional or even global scale. Therefore, the results of this study may also be useful in improving our understanding of aerosol climate effects in the surface–atmosphere system.

Nonetheless, some uncertainties remain in our results, and these should be highlighted. Because the calculations of all-sky ADRF need both satellite-based aerosol and cloud data as inputs to the SBDART model, which are difficult to acquire, only clear-sky ADRF is calculated in the present work. Therefore, on the one hand this causes some differences between our results and the all-sky ADRF results in previous studies; while on the other hand it means that uncertainties still exist in relating the ADRF pattern or trend to real general circulation (monsoon year) cases, because clear-sky ADRF is only an assumed condition. Compared to clear-sky ADRF, all-sky ADRF, which involves cloud, should be more suitable in investigating the interactions between aerosols and monsoon circulation. Therefore, work on the calculation of grid-cell all-sky ADRF will be conducted in the future by using a column radiative model together with aerosol and cloud observations from multiple satellite and in-situ sources.

Finally, it is also worth noting that, relative to previous simulations of aerosol radiative effects performed at the site scale and based on radiation transfer models with inputs from a small number of ground-based sites, our study is the first to combine observations from satellites, ground-based networks, meteorological fields and a radiative transfer model to reveal the spatial and temporal variations of grid-cell ADRF in EC. However, the number of AERONET sites in EC is limited, and their observations are not continuous. As more new sites are built and more measurements are obtained, continuous research at longer time scales and over an extended area should be conducted in future work.

Acknowledgements. We appreciate the comments and suggestions of the editors and anonymous reviewers. We thank the AERONET principal investigators and their staff for establishing and maintaining the AERONET sites used in this investigation. This work is supported by the Chinese Academy of Sciences Strategic Priority Research Program (Grant No. XDA05100303), the National Natural Science Foundation of China (Grant Nos. 41230419, 91337213 and 41075041), and the Special Funds for Public Welfare of China (Grant No. GYHY201306077).

REFERENCES

Bellouin, N., J. Quaas, J.-J. Morcrette, and O. Boucher, 2013: Estimates of aerosol radiative forcing from the MACC reanalysis. *Atmos. Chem. Phys.*, **13**(4), 2045–2062.

Charlson, R. J., S. E. Schwartz, J. M. Hales, R. D. Cess, J. A. Coakley, Jr., J. E. Hansen, and D. J. Hofmann, 1992: Climate forcing by anthropogenic aerosols. *Science*, **255**(5043), 423–430.

Chen, H., X. F. Gu, T. H. Cheng, T. Yu, and Z. Q. Li, 2013: Characteristics of aerosol types over China. *Journal of Remote Sensing*, **17**(6), 1559–1571.

Cheng, Z., and Coauthors, 2014: Impact of biomass burning on haze pollution in the Yangtze River delta, China: A case study in summer 2011. *Atmos. Chem. Phys.*, **14**(9), 4573–4585.

Dubovik, O., and M. D. King, 2000: A flexible inversion algorithm for retrieval of aerosol optical properties from Sun and sky radiance measurements. *J. Geophys. Res.*, **105**(D16), 20 673–

20 696.

Dubovik, O., A. Smirnov, B. N. Holben, M. D. King, Y. J. Kaufman, T. F. Eck, and I. Slutsker, 2000: Accuracy assessments of aerosol optical properties retrieved from Aerosol Robotic Network (AERONET) Sun and sky radiance measurements. *J. Geophys. Res.*, **105**(D8), 9791–9806.

Dubovik, O., B. Holben, T. F. Eck, A. Smirnov, Y. J. Kaufman, M. D. King, D. Tanré, and I. Slutsker, 2002: Variability of absorption and optical properties of key aerosol types observed in worldwide locations. *J. Atmos. Sci.*, **59**(3), 590–608.

Han, Z. W., R. J. Zhang, Q. G. Wang, W. Wang, J. J. Cao, and J. Xu, 2008: Regional modeling of organic aerosols over China in summertime. *J. Geophys. Res.*, **113**(D11), doi: 10.1029/2007JD009436.

Haywood, J. M., and K. P. Shine, 1997: Multi-spectral calculations of the direct radiative forcing of tropospheric sulphate and soot aerosols using a column model. *Quart. J. Roy. Meteor. Soc.*, **123**(543), 1907–1930.

Holben, B. N., and Coauthors, 1998: AERONET-A federated instrument network and data archive for aerosol characterization. *Remote Sensing of Environment*, **66**(1), 1–16.

Jones, A., D. L. Roberts, and A. Slingo, 1994: A climate model study of indirect radiative forcing by anthropogenic sulphate aerosols. *Nature*, **370**, 450–453.

Ju, L.-X., and Z.-W. Han, 2013: Impact of different east Asian summer monsoon circulations on aerosol-induced climatic effects. *Atmos. Oceanic Sci. Lett.*, **6**(5), 227–232.

Kaufman, Y. J., D. Tanré, and O. Boucher, 2002: A satellite view of aerosols in the climate system. *Nature*, **419**(6903), 215–223.

Kaufman, Y. J., I. Koren, L. A. Remer, D. Rosenfeld, and Y. Rudich, 2005: The effect of smoke, dust, and pollution aerosol on shallow cloud development over the Atlantic Ocean. *Proceedings of the National Academy of Sciences of the United States of America*, **102**(32), 11 207–11 212.

Kim, S.-W., S.-C. Yoon, J. Kim, and S.-Y. Kim, 2007: Seasonal and monthly variations of columnar aerosol optical properties over east Asia determined from multi-year MODIS, LIDAR, and AERONET Sun/sky radiometer measurements. *Atmos. Environ.*, **41**(8), 1634–1651.

Levy, R. C., L. A. Remer, R. G. Kleidman, S. Mattoo, C. Ichoku, R. Kahn, and T. F. Eck, 2010: Global evaluation of the Collection 5 MODIS dark-target aerosol products over land. *Atmos. Chem. Phys.*, **10**(21), 10 399–10 420.

Li, C. C., J. T. Mao, K.-H. A. Lau, J.-C. Chen, Z. B. Yuan, X. Y. Liu, A. H. Zhu, and G. Q. Liu, 2003: Characteristics of distribution and seasonal variation of aerosol optical depth in eastern China with MODIS products. *Chinese Science Bulletin*, **48**(22), 2488–2495.

Li, J. P., and Q. C. Zeng, 2002: A unified monsoon index. *Geophys. Res. Lett.*, **29**(8), 115-1–115-4.

Li, Z. Q., and Coauthors, 2007: Aerosol optical properties and their radiative effects in northern China. *J. Geophys. Res.*, **112**(D22), doi: 10.1029/2006JD007382.

Li, Z. Q., K.-H. Lee, Y. S. Wang, J. Y. Xin, and W.-M. Hao, 2010: First observation-based estimates of cloud-free aerosol radiative forcing across China. *J. Geophys. Res.*, **115**(D7), doi: 10.1029/2009JD013306.

Liao, L., S. J. Lou, Y. Fu, W. Y. Chang, and H. Liao, 2015: Radiative forcing of aerosols and its impact on surface air temperature on the synoptic scale in eastern China. *Chinese Journal of Atmospheric Sciences*, **39**(1), 68–82. (in Chinese)

Lyapustin, A., and Coauthors, 2014: Scientific impact of MODIS C5 calibration degradation and C6+ improvements. *Atmospheric Measurement Techniques*, **7**, 4353–4365.

Mao, J. T., J. H. Zhang, and M. H. Wang, 2002: Summary comment on research of atmospheric aerosol in China. *Acta Meteorologica Sinica*, **60**(5), 625–634. (in Chinese)

Menon, S., J. Hansen, L. Nazarenko, and Y. F. Luo, 2002: Climate effects of black carbon aerosols in China and India. *Science*, **297**(5590), 2250–2253.

Myhre, G., and Coauthors, 2013: Radiative forcing of the direct aerosol effect from AeroCom Phase II simulations. *Atmos. Chem. Phys.*, **13**(4), 1853–1877.

Ramanathan, V., P. J. Crutzen, J. T. Kiehl, and D. Rosenfeld, 2001: Aerosols, climate, and the hydrological cycle. *Science*, **294**(5549), 2119–2124.

Ricchiazzi, P., S. R. Yang, C. Gautier, and D. Sowle, 1998: SBDART: A research and teaching software tool for plane-parallel radiative transfer in the Earth's atmosphere. *Bull. Amer. Meteor. Soc.*, **79**(10), 2101–2114.

Rosenfeld, D., J. Dai, X. Yu, Z. H. Yao, X. H. Xu, X. Yang, and C. L. Du, 2007: Inverse relations between amounts of air pollution and orographic precipitation. *Science*, **315**(5817), 1396–1398.

Shi, G. Y., B. Wang, H. Zhang, J. Q. Zhao, S. C. Tan, and T. X. Wen, 2008: The radiative and climatic effects of atmospheric aerosols. *Chinese Journal of Atmospheric Sciences*, **32**(4), 826–840. (in Chinese)

Sundström, A.-M., A. Arola, P. Kolmonen, Y. Xue, G. de. Leeuw, and M. Kulmala, 2015: On the use of a satellite remote-sensing-based approach for determining aerosol direct radiative effect over land: A case study over China. *Atmos. Chem. Phys.*, **15**(1), 505–518.

Wang, X. H., G. Y. Shi, and X. Y. Ma, 2002: The Direct Radiative Forcing of anthropogenic Sulfate and its temperature response over Eastern Asia. *Chinese Journal of Atmospheric Sciences*, **26**(6), 751–760. (in Chinese)

Wang, Y., H. Z. Che, J. Z. Ma, Q. Wang, G. Y. Shi, H. B. Chen, P. Goloub, and X. J. Hao, 2009: Aerosol radiative forcing under clear, hazy, foggy, and dusty weather conditions over Beijing, China. *Geophys. Res. Lett.*, **36**(6), doi: 10.1029/2009GL037181.

Wu, G. X., and Coauthors, 2016: Advances in studying interactions between aerosols and monsoon in China. *Science China Earth Sciences*, **59**, 1–16, doi: 10.1007/s11430-015-5198-z.

Xia, X., and Coauthors, 2016: Ground-based remote sensing of aerosol climatology in China: Aerosol optical properties, direct radiative effect and its parameterization. *Atmos. Environ.*, **124**, 243–251.

Xia, X., H. Chen, P. Goloub, W. Zhang, B. Chatenet, and P. Wang, 2007a: A compilation of aerosol optical properties and calculation of direct radiative forcing over an urban region in northern China. *J. Geophys. Res.*, **112**(D2), doi: 10.1029/2006JD008119.

Xia, X. G., Z. Q. Li, B. Holben, P. C. Wang, T. Eck, H. B. Chen, M. Cribb, and Y. X. Zhao, 2007b: Aerosol optical properties and radiative effects in the Yangtze Delta region of China. *J. Geophys. Res.*, **112**(D22), doi: 10.1029/2007JD008859.

Zhang, H., S. Y. Zhao, Z. L. Wang, X. Y. Zhang, and L. C. Song, 2016: The updated effective radiative forcing of major anthropogenic aerosols and their effects on global climate at present and in the future. *Int. J. Climatol.*, **36**, 4029–4044, doi: 10.1002/joc.4613.

Zhang, L., H. Liao, and J. P. Li, 2010: Impacts of Asian summer monsoon on seasonal and interannual variations of aerosols over eastern China. *J. Geophys. Res.*, **115**(D7), doi: 10.1029/2009JD012299.

Zhang, Q. Y., S. Y. Tao, and L. T. Chen, 2003: The inter-annual variability of East Asian summer monsoon indices and its association with the pattern of general circulation over East Asia. *Acta Meteorologica Sinica*, **61**(4), 559–568. (in Chinese)

Zhang, X. Y., P. Zhang, Y. Zhang, X. J. Li, and H. Qiu, 2007: The trend, seasonal cycle, and sources of tropospheric NO_2 over China during 1997–2006 based on satellite measurement. *Science in China Series D*: *Earth Sciences*, **50**(12), 1877–1884.

Zhao, C. S., and Coauthors, 2006a: Aircraft measurements of cloud droplet spectral dispersion and implications for indirect aerosol radiative forcing. *Geophys. Res. Lett.*, **33**(16), doi: 10.1029/2006GL026653.

Zhao, C. S., X. X. Tie, and Y. P. Lin, 2006b: A possible positive feedback of reduction of precipitation and increase in aerosols over eastern central China. *Geophys. Res. Lett.*, **33**(11), doi: 10.1029/2006GL025959.

Zhao, C., L. R. Leung, R. Easter, J. Hand, and J. Avise, 2013a: Characterization of speciated aerosol direct radiative forcing over California. *J. Geophys. Res.*, **118**(5), 2372–2388.

Zhao, C., and Coauthors, 2013b: A sensitivity study of radiative fluxes at the top of atmosphere to cloud-microphysics and aerosol parameters in the community atmosphere model CAM5. *Atmos. Chem. Phys.*, **13**(21), 10 969–10 987.

Zheng, X. Y., Y. F. Fu, Y. J. Yang, and G. S. Liu, 2015: Impact of atmospheric circulations on aerosol distributions in autumn over eastern China: Observational evidence. *Atmos. Chem. Phys.*, **15**(21), 12 115–12 138.

Zhu, J. L., H. Liao, and J. P. Li, 2012: Increases in aerosol concentrations over eastern China due to the decadal-scale weakening of the East Asian summer monsoon. *Geophys. Res. Lett.*, **39**(9), doi: 10.1029/2012GL051428.

Zhu, Y. F., 2008: An index of East Asian winter monsoon applied to description the Chinese mainland winter temperature changes. *Acta Meteorologica Sinica*, **66**(5), 781–788. (in Chinese)